

High spin-wave asymmetry and emergence of radial standing modes in thick ferromagnetic nanotubes

R. A. Gallardo,^{1,2,*} P. Alvarado-Seguel,¹ and P. Landeros^{1,2}

¹*Departamento de Física, Universidad Técnica Federico Santa María, Avenida España 1680, Valparaíso, Chile*

²*Center for the Development of Nanoscience and Nanotechnology (CEDENNA), 917-0124 Santiago, Chile*



(Received 25 January 2022; accepted 14 March 2022; published 31 March 2022)

Magneto-chiral properties are enriched in curved magnetic nanostructures, in which dipole-dipole and exchange couplings are their physical sources. In such systems, direct implications are evidenced in the magnetization dynamics, where a noticeable frequency shift appears between two counterpropagating spin waves. In this paper, the spin-wave asymmetry induced by the curvature is theoretically studied in thick ferromagnetic nanotubes with a vortex ground state. The spin-wave spectra are obtained using semianalytical calculations and the dynamical matrix method for thin and thick nanotubes. Under the thickness increase, radial standing spin waves are observed at low frequencies, while the nonreciprocal properties are improved. Such standing waves exhibit a nonreciprocal spin-wave dispersion, but it is not as prominent as the asymmetry of the low-frequency in-phase modes. In the limit of small wave vectors, analytical expressions are reported for the spin-wave dispersion, where the resonance frequency, the frequency shift of two counterpropagating waves, and the critical field that destabilizes the vortex state are determined. The obtained frequency shift allows us to estimate the influence of thickness and curvature on the nonreciprocity of the spin waves. These results constitute a significant advance in the fundamental understanding of the spin-wave dynamics of ferromagnetic nanotubes, predicting new phenomena and providing expressions that are easy to interpret and that allow us, therefore, to promote the study of magnetization dynamics in curved structures.

DOI: [10.1103/PhysRevB.105.104435](https://doi.org/10.1103/PhysRevB.105.104435)

I. INTRODUCTION

Due to their curved surface and reduced nanometer size, together with the competition among magnetic energies, the magnetic properties of nanotubes (NTs) are unique [1,2]. For example, the ubiquitous curling magnetization that wraps a cylindrical crust appears in different magnetic textures to reduce the demagnetizing energy and leads to magneto-chiral properties [3–8]. The occurrence of different magnetic states and reversal paths depends strongly on the tube's cross-section and length [2,9–13], as well as on the material and quality of the structure [14–19]. The magnetization almost aligns with the tube axis for long nanotubes with a radius (R) less than a few exchange lengths [9]. For slightly more significant R , the dipolar term becomes relevant, and the magnetization at the tube boundaries prefers to develop vortex domains to reduce such energy term [9,20,21], while for an even larger radius, a flux-closure vortex state appears [22]. In the case of solid cylindrical nanowires, it has been shown that the presence of magnetic matter at the symmetry axis causes a Bloch-point singularity [23–25], which complicates the reversal processes. In the nanotube, the inner void eludes the formation of Bloch points, facilitating the domain-wall-based reversal process and leading to ultrafast chiral domain walls [3,26]. Moreover, magnetic NTs are potential candidates for

biomedical applications, which principally includes imaging, sensing, drug delivery, and magnetic hyperthermia [27–30].

The spin waves (SWs) are the elementary magnetic excitations behind the rising field of magnonics [31], which has been active for around 90 years, since the prediction of the spin excitations by Bloch and further discovery of ferromagnetic resonance in metals [32]. Spin waves can carry information, and they are essential for low-consumption information technologies. They usually propagate reciprocally in frequency but with different amplitudes in a thick film [33]. However, under given conditions, two counterpropagating waves exhibit different wavelengths at the same frequency, thus producing an asymmetric wave dispersion. See the discussion about spin-wave nonreciprocity in Chap. 16 of Ref. [31]. In magnetic materials, this asymmetry in the SW dispersion has been observed in different types of systems, such as coupled ferromagnetic bilayers [34–42], magnetization-graded films [42,43], magnetic nanotubes [44–47], arrays of nanopillars [48], noncentrosymmetric crystals [49–52], heavy-metal/ferromagnetic interfaces [53–58], and magnonic crystals [59,60]. Due to the peculiar characteristics of the nonreciprocal waves, potential magnonic applications such as circulators, isolators, phase shifters, diodes, and logic devices have been envisioned [61,62].

In ferromagnetic thin films coupled with a heavy metal (a material with strong spin-orbit coupling), the source of the SW nonreciprocity is the antisymmetric exchange known as Dzyaloshinskii-Moriya (DM) interaction [63–65], which introduces an additional term in the SW dispersion that varies

*rodolfo.gallardo@usm.cl

linearly with the wave vector [50,51]. Nevertheless, due to the interfacial nature of the DM energy, the SW asymmetry is not observed in thick FM films since the DM strength decays as the inverse of the thickness [56,58]. On the other side, when the classical dipole-dipole interaction causes the magnonic nonreciprocity, the dependence with the thickness changes since the frequency shift Δf (frequency difference of two counterpropagating waves evaluated at the same magnitude of the wave vector) increases with the FM layer thickness. Indeed, a giant increment of Δf based on the dipole-dipole coupling has been predicted to occur in magnetization-graded films [42,43], ferromagnetic nanotubes [44–46], and anti-ferromagnetically coupled bilayers [38–41]. In the coupled bilayers, the dynamic dipolar interaction between the two FM layers depends strongly on the wave-vector sign, thus inducing a notable nonreciprocity that increases with the layer thicknesses [38].

Early studies of magnetic excitations in ferromagnetic NTs focused on calculating the dispersion relation where elliptically polarized waves appeared from the competition between exchange and magnetostatic interactions [66]. Experimental and theoretical research has been carried out in cylindrical nanowires [67,68], short nanorings structures [20,69,70], microtubes [71–73], long nanotubes [70,74,75], coupled cylindrical multilayers [76], and tubes with rectangular [77] and hexagonal cross section [78,79]. The calculation of spin excitations in an ultrathin nanotube hosting a vortex domain wall texture resulted in scattered waves by the wall (with an associated phase shift) and an increment in the magnonic band gap [74]. However, the authors in Ref. [74] did not find nonreciprocal wave propagation, perhaps because the dispersion of backward-volume SWs is reciprocal for a static magnetization along the axis or because the theory considered the dipole term in a local thin-film approach, where magnetochiral effects vanish [3,6]. Nonetheless, in thin magnetic nanotubes (NTs) with a vortex magnetization ground state, a notable SW asymmetry has been predicted for waves propagating along the tube [44–46]. Here, it has been theoretically demonstrated by numerical calculations and micromagnetic simulations that the dynamic dipolar interaction causes nonreciprocal spin-wave dispersion for the zeroth-order and higher-order azimuthal modes [45]. Further micromagnetic studies of the dynamic modes in NTs excited by rotating magnetic fields evidence an asymmetric ferromagnetic resonance and azimuthal SW modes at the resonant frequencies of the rotating fields [80,81]. The experimental proof of the asymmetric SW dispersion has been recently reported in hexagonal permalloy nanotubes measured with time-resolved scanning transmission x-ray microscopy [47].

Due to the characteristics of dipole-dipole coupling, the spin-wave asymmetry depends strongly on the tube radius and its thickness. Indeed, the nonreciprocity becomes prominent as the thickness of the NT increases [45]. Therefore, it is interesting to study thick nanotubes, where such a thickness can be several times larger than the exchange length. Nonetheless, the analysis for thick NTs must consider the inhomogeneous radial profile of the dynamic magnetization, which has not been calculated so far in systems with a tubular cross-section in a vortex ground state. See Refs. [67,68] for a full description of spin dynamics in axially magnetized cylin-

drical wires that correctly incorporates magnetostatics with its radial dependence. Furthermore, in the small wave-vector regime, there are not fully analytical expressions for the SW dispersion or frequency shift in nanotubes, since only semi-analytical formulas have been derived, all of which require us to carry out one or more numerical integrations [44,45]. Therefore, practical analytical expressions are highly desired in this context since they allow easy analysis of the dynamic behavior of the spin waves as a function of the geometrical and magnetic parameters of the system.

In this paper, the spin-wave dynamics of thick ferromagnetic nanotubes are theoretically studied. The ground state of the tubular system is assumed to be a vortex configuration, while the SWs propagate along the nanotube axis. Two methods are used to calculate the SW spectra. The first one calculates the magnonic modes (including the higher-order azimuthal modes) of a thin NT, where the magnetostatic coupling is treated in its nonlocal form. Then, the dynamic matrix method (DMM) is employed to calculate the temporal evolution of the magnetization for thick NTs. Thus, the theoretical methods allow calculating both the azimuthal and radial standing SW modes, where the radial modes are observed at lower frequencies as the thickness of the nanotube increases. The SW nonreciprocity is also observed, where an enhancement of the SW asymmetry is obtained as the NT thickness increases, but principally for the low-frequency in-phase mode. The small wave-vector limit is analyzed to get a deeper insight into the SW asymmetry induced by the dipolar field and the curvature, where fully analytical expressions for the spin-wave dispersion and the critical magnetic field destabilizing the vortex state are derived.

II. THEORY

A ferromagnetic nanotube with R (a) being the outer (inner) radius and $d = R - a$ the thickness is shown in Fig. 1. Here an equilibrium vortex state is assumed, which can occur naturally for certain sizes [9] or may also be induced with an electric current in an inner conductor and its associated circular field [82]. The dynamic matrix method is applied to obtain the SW spectra for thick NTs [83–85]. This method dictates the subdivision of one nanotube into N cylindrical layers coupled by exchange and dipolar interactions (see Fig. 1). Each cylindrical shell, say the n th one, has thickness $\zeta = d/N$, inner radius $r(n) = a + (n - 1)\zeta$, and outer radius $r(n + 1)$. Thereby, the magnetization dynamics of thick nanotubes can be described correctly since the method considers the radial modulation of the dynamic magnetization.

The temporal evolution of the n th cylindrical layer is described by the Landau-Lifshitz (LL) equation,

$$\frac{d}{dt}\mathbf{M}^n(\mathbf{r}, t) = -\mu_0\gamma\mathbf{M}^n(\mathbf{r}, t) \times \mathbf{H}^n(\mathbf{r}, t), \quad (1)$$

where \mathbf{M}^n is its magnetization, \mathbf{H}^n is the effective field acting on the n th layer, and γ is the absolute value of the gyromagnetic ratio. Monochromatic plane waves propagating along the z -axis will be assumed. In the linear-response regime, both the magnetization and the effective field can be written as $\mathbf{M}^n(\mathbf{r}, t) = \mathbf{M}_{\text{eq}}^n(\varphi) + \mathbf{m}^n(\varphi)e^{i(\mathbf{k}\cdot\mathbf{r}+l\varphi-\omega t)}$ and $\mathbf{H}^n(\mathbf{r}, t) = \mathbf{H}_{\text{eq}}^n(\varphi) + \mathbf{h}^n(\varphi)e^{i(\mathbf{k}\cdot\mathbf{r}+l\varphi-\omega t)}$, where $\mathbf{M}_{\text{eq}}^n(\varphi) =$

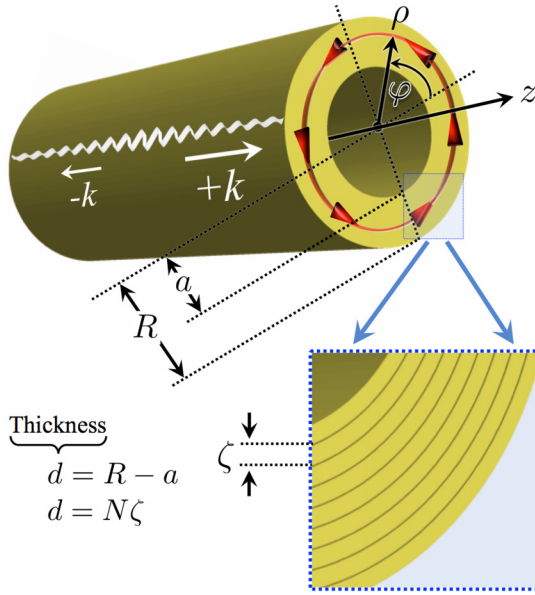


FIG. 1. Thick nanotube system. The spin waves propagate along the nanotube, while the equilibrium magnetization describes a vortex ground state. Parameters a and R denote the inner and outer radius, respectively. The coordinate system and the spin-wave propagation directions are schematically illustrated. The thickness of the nanotube is given by $d = R - a = N\zeta$, with ζ being the thickness of the n th cylindrical layer and N the total number of layers.

$M_s^n \hat{\phi}$ and $\mathbf{m}^n(\varphi) = m_z \hat{\mathbf{z}} + m_\rho \hat{\rho}$, similarly for the effective field. Here, M_s^n is the saturation magnetization of the n th layer, $\mathbf{k} = k \hat{\mathbf{z}}$ is the wave vector, $\omega = 2\pi f$ is the angular frequency, and l is an integer associated with the quantization of the azimuthal standing modes [67,68]. Thus, the linearized equation of motion (1) becomes

$$\omega \mathbf{m}^n = i\gamma \mu_0 (\mathbf{H}_{\text{eq}}^n \times \mathbf{m}^n + \mathbf{h}^n \times \mathbf{M}_{\text{eq}}^n) \quad (2)$$

for $1 \leq n \leq N$. The dynamic effective fields can be written as a linear combination of the dynamic magnetization components, namely $\mathbf{h}^n = -\sum_p \Lambda^{np} \cdot \mathbf{m}^p$. Therefore, once the dynamic tensors $\Lambda^{np} = \Lambda_u^{np} + \Lambda_{\text{ex}}^{np} + \Lambda_{\text{dip}}^{np}$ and static fields $\mathbf{H}_{\text{eq}}^n(\varphi) = \mathbf{H}_Z(\varphi) + \mathbf{H}_{\text{ex}}^n(\varphi)$ are calculated, Eq. (2) can be solved as an eigenvalue problem. Note that Λ_u^{np} , Λ_{ex}^{np} , and $\Lambda_{\text{dip}}^{np}$ are associated with the uniaxial, exchange, and dipolar interaction, respectively. In the case of Zeeman interaction, an external circular field $\mathbf{H}_Z(\varphi) = H_0 \hat{\phi}$ will be assumed, which may originate with an electric current in an inner conductor wire [44]. In contrast, for anisotropy the associated field is given by $\mathbf{h}_u^n = [2K_u/(\mu_0 M_s^2)] m_z^n \hat{\mathbf{z}}$. Hence, $\Lambda_u^{np} = -\delta_{np} [2K_u/(\mu_0 M_s^2)] \hat{\mathbf{z}} \otimes \hat{\mathbf{z}}$, with \otimes denoting the tensor product. To stabilize the vortex equilibrium state, a negative uniaxial anisotropy constant will be used ($K_u < 0$).

On the other hand, the exchange interaction is accounted for employing two terms. One of them is associated with the exchange coupling within each nanotube. This inner exchange field is $\mathbf{H}_{\text{ex}}^n = \ell_{\text{ex}}^2 \nabla^2 \mathbf{M}^n$, where $\ell_{\text{ex}} = (2A_{\text{ex}}/\mu_0 M_s^2)^{1/2}$ is the exchange length, and A_{ex} is the exchange constant. However, since this field depends on the radial coordinate ρ , the radial average of the effective exchange field is calculated, namely $\mathbf{H}_{\text{ex}}^n = (\int \ell_{\text{ex}}^2 \nabla^2 \mathbf{M}^n d\rho)/\zeta$, with integration

limits from $r(n)$ to $r(n+1)$. The other term is related to the exchange interaction between neighboring cylindrical layers. In this case, the exchange energy density (energy/length) between two neighboring layers is $\epsilon_{\text{ex}}^{np} = -[J_{\text{ex}}^{np}/(M_s^n M_s^p)] \mathbf{M}^n \cdot \mathbf{M}^p$, wherein J_{ex}^{np} is a coupling parameter. Then, the effective field is derived from $\mathbf{H}^n = -\sum_p (\delta \epsilon_{\text{ex}}^{np}/\delta \mathbf{M}^n)/[\mu_0 S(n)]$, where $S(n) = \pi[r(n+1)^2 - r(n)^2]$ is the cross section of the n th layer. Taking into account both exchange contributions, it follows that

$$\mathbf{H}_{\text{eq-ex}}^n(\varphi) = \left(\sum_p \frac{J_{\text{ex}}^{np}}{\mu_0 S(n) M_s^n} - \frac{\ell_{\text{ex}}^2 M_s^n}{r(n)r(n+1)} \right) \hat{\phi} \quad (3)$$

and

$$\Lambda_{\text{ex}}^{np} = \delta_{np} \ell_{\text{ex}}^2 \left(\frac{\hat{\rho} \otimes \hat{\rho} + l^2 \mathbf{I}}{r(n)r(n+1)} + k^2 \mathbf{I} \right) - \frac{J_{\text{ex}}^{np}}{\mu_0 S(n) M_s^n M_s^p} \mathbf{I}, \quad (4)$$

where \mathbf{I} is the identity matrix. In the continuous approach, keeping in mind that there will be many coupled cylindrical shells, it is straightforward to show that $J_{\text{ex}}^{np} = 2A_{\text{ex}}[2\pi r[(n+1)/2]]/\zeta$ [86]. It is worth mentioning that the exchange interaction in curved structures can be written in three categories containing isotropic exchange, chiral parts, and anisotropic parts. In the present case, isotropic and anisotropic parts are obtained, while chiral terms are null. This result is in concordance with Ref. [6], where it is shown that the circular nanotube geometry has zero chiral terms driven by exchange, due to its constant radius of curvature. However, for the particular case of an elliptical nanotube with a variable radius of curvature, a chiral term originating from the exchange coupling is expected [6].

The dipole-dipole interaction is now calculated. The magnetic field due to the p th tubular layer is given by

$$\mathbf{H}_{\text{dip}}^{(p)}(\mathbf{r}, t) = \frac{\nabla}{4\pi} \left(\int \frac{\nabla' \cdot \mathbf{M}^p(\mathbf{r}', t)}{|\mathbf{r} - \mathbf{r}'|} dV' \right) \quad (5)$$

$$- \oint \frac{\hat{\mathbf{n}}' \cdot \mathbf{M}^p(\mathbf{r}', t)}{|\mathbf{r} - \mathbf{r}'|} da'. \quad (6)$$

Notice the difference in notation between \mathbf{H}^p and $\mathbf{H}^{(p)}$. The former denotes the effective field acting on the p th tubular layer, while the latter refers to the field produced by the p th layer. Due to the vortex configuration of the equilibrium magnetization, the static dipolar field is zero [87]. Indeed,

$$\nabla \cdot \mathbf{M}^p(\mathbf{r}, t) = (ikm_z + m_\rho/\rho) e^{i(\mathbf{k} \cdot \mathbf{r} + l\varphi - \omega t)}, \quad (7)$$

$$\hat{\mathbf{n}} \cdot \mathbf{M}^p(\mathbf{r}, t) = \text{sgn}[\rho - r(p+1/2)] m_\rho e^{i(\mathbf{k} \cdot \mathbf{r} + l\varphi - \omega t)}, \quad (8)$$

where the term m_ρ/ρ corresponds to the contribution from the geometrical magnetic charge that emerges from curvature [6]. Hence, $\mathbf{H}_{\text{dip}}^{(p)}(\mathbf{r}, t) = \mathbf{h}_{\text{dip}}^{(p)}(\rho, \varphi) e^{i(\mathbf{k} \cdot \mathbf{r} + l\varphi - \omega t)}$. Now, the demagnetizing tensor $\Lambda_{\text{dip}}^{np}$ is defined with the radial average on the n th layer, namely

$$\frac{1}{\zeta} \int \mathbf{h}_{\text{dip}}^{(p)}(\rho, \varphi) d\rho = -\Lambda_{\text{dip}}^{np} \cdot \mathbf{m}^p(\varphi), \quad (9)$$

where the integral goes from $r(n)$ to $r(n+1)$ in such a way that the dipolar field $\mathbf{h}_{\text{dip}}^{(p)}(\rho, \varphi)$ due to the p th cylindrical layer is averaged into the n th layer. Then, it follows that

$$(\Lambda_{\text{dip}}^{np})_{\rho\rho} = \iiint \rho' \partial_{\rho\rho'} G(\rho, \rho', \varphi') d\rho d\rho' d\varphi', \quad (10a)$$

$$(\Lambda_{\text{dip}}^{np})_{z\rho} = ik \iiint \rho' \partial_{\rho'} G(\rho, \rho', \varphi') d\rho d\rho' d\varphi', \quad (10b)$$

$$(\Lambda_{\text{dip}}^{np})_{\rho z} = -ik \iiint \rho' \partial_{\rho} G(\rho, \rho', \varphi') d\rho d\rho' d\varphi', \quad (10c)$$

$$(\Lambda_{\text{dip}}^{np})_{zz} = k^2 \iiint \rho' G(\rho, \rho', \varphi') d\rho d\rho' d\varphi', \quad (10d)$$

where the ρ' -integrals go from $r(p)$ to $r(p+1)$, the ρ -integrals go from $r(n)$ to $r(n+1)$, the φ' -integrals go from 0 to 2π , and

$$G(\rho, \rho', \varphi') = \frac{e^{i\ell\varphi'}}{2\pi\zeta} K_0(|k|\sqrt{\rho^2 + \rho'^2 - 2\rho\rho' \cos \varphi'}). \quad (11)$$

Equations (10) follow from writing (7) in polar coordinates, using the identity $\int_{-\infty}^{\infty} dz e^{ik\cdot\mathbf{r}'}/|\mathbf{r}-\mathbf{r}'| = 2K_0(|k||\rho-\rho'|)e^{ik\cdot\mathbf{r}}$ to solve the z' integrals, noting that the φ' -integrals are invariant under $\varphi' \mapsto \varphi' + \varphi$, correctly identifying the $\Lambda_{\text{dip}}^{np}$ components from (9), and then doing integration by parts where appropriate. In Eq. (11), K_0 denotes the zeroth modified Bessel function of the second kind. The coefficients (10a) and (10b) describe the contribution of the superficial and geometric magnetic charges to the demagnetization tensor (they are mixed due to the integration by parts), while (10c) and (10d) describe the contribution of the bulk magnetic charges. It is also worth mentioning that if $n = p$, the φ' -integrals have to be realized as $\lim_{\epsilon \rightarrow 0^+} \int_{\epsilon}^{2\pi-\epsilon} d\varphi'$ to avoid the singularities at $\rho = \rho'$. In the following sections, different approaches to solve Eq. (10) are discussed, which are based on (i) numerical integrations, (ii) the ultrathin approach, (iii) the ultrathin approach plus the dynamic matrix method, and (iv) the small wave-vector limit.

A. Numerical integration

In the case of only one cylindrical layer ($N = 1$), the SW dynamics can be described by solving the integrals shown in Eq. (10) numerically. Of course, this solution is limited to thin nanotubes since, for $N = 1$, the radial profiles of the dynamic magnetization components are assumed to be homogeneous. For instance, the SW spectra of NTs with a thickness lower than 10 nm can be correctly calculated. On the other side, to calculate the magnon spectra of thick NTs, the dynamic matrix method can be used. Nevertheless, because the DMM requires the calculations of the SW dynamics of coupled tubular layers ($N > 1$), the complete numerical integration associated with the coordinates ρ , ρ' , and φ' is not a good choice from a computational viewpoint. Thus, to reduce the computation time and to allow the magnetization to change along the tube thickness, other approaches are presented in what follows.

B. Ultrathin approach

In the case of one ultrathin nanotube ($d < \ell_{\text{ex}}$), the integrals depicted in Eq. (10) that are associated with the dipolar energy can be solved in a more simplified way. Because slight variations of the dynamic magnetization components are expected along the NT thickness for the ultrathin shell, the numerical radial integrals can be done by using a midpoint approach, where ρ is replaced by the midpoint of the interval $[a, a + \zeta]$. Namely, $\rho = r(3/2) = a + \zeta/2$. Thereby, the SW spectra are now calculated by carrying out only one numerical integration on the variable φ' . Of course, the ultrathin approach will be valid for a thickness lower than the exchange length of the nanostructure. If the thickness of the NT increases, the dipolar field is less uniform within the nanotube, and hence the midpoint approximation fails, which becomes more evident at large wave vectors where the dipolar interaction is enhanced.

C. Ultrathin approach plus dynamic matrix method

According to the DMM, the thick nanotube is divided into many cylindrical layers so that each one is ultrathin ($\zeta \approx 1$ nm), and one can correctly describe tubes beyond the ultrathin approach. Therefore, similar to the previous case, the ρ and ρ' integrals are approximated by replacing $\rho = r(n + 1/2)$ and $\rho' = r(p + 1/2)$, respectively. Thus, the spin-wave dispersion can be calculated once the numerical integration on the variable φ' is realized for each shell. The main advantage of using the ultrathin approach plus DMM is that the dynamic properties of thick NTs can now be calculated without significant computational efforts since the radial integrations have been avoided by utilizing the midpoint approach.

D. Small wave-vector limit

It is also feasible to obtain analytical expressions for the SW dispersion at the limit of small wave vectors for the case of one NT ($N = 1$) and $l = 0$. In this case, the Bessel function is expanded as $K_0(z) = -\alpha_E - \ln(z/2) + O(z)^2$, where $\alpha_E \approx 0.577$ stands for the Euler-Mascheroni constant. Thus, matrix $\Lambda_{\text{dip}}^{11}$ is solved analytically, so that $(\Lambda_{\text{dip}}^{11})_{\rho\rho} = 1$, $(\Lambda_{\text{dip}}^{11})_{z\rho} = -ik(\mathcal{A}_+ - \mathcal{A}_-) = -ikd/2$, $(\Lambda_{\text{dip}}^{11})_{\rho z} = ik(\mathcal{A}_+ + \mathcal{A}_-) = ik\frac{R+a}{4} \ln(\frac{R}{a})$, and $(\Lambda_{\text{dip}}^{11})_{zz} = -k^2\mathcal{B}(k)$. Here, the following functions have been defined:

$$\mathcal{A}_{\pm} = \frac{1}{8} \left[(a+R) \ln\left(\frac{R}{a}\right) \pm 2d \right] \quad (12)$$

and

$$\mathcal{B}(k) = \frac{1}{8d} \left\{ 4a^3 \ln\left(\frac{|k|a}{2}\right) + 4R^3 \ln\left(\frac{|k|R}{2}\right) + (a+R) \times \left[(4\alpha_E - 3)d^2 - 2aR \ln\left(\frac{k^2 aR}{4}\right) \right] \right\}. \quad (13)$$

After some algebraic manipulations, the SW dispersion becomes

$$f_{\text{an}}(k) = \frac{\gamma\mu_0 M_s}{2\pi} \left[kA_+ + \sqrt{k^2 A_-^2 + \left(1 + k^2 \ell_{\text{ex}}^2 + \frac{H_0}{M_s}\right) \left(\frac{H_0}{M_s} - \frac{2K_u}{\mu_0 M_s^2} - \frac{\ell_{\text{ex}}^2}{aR} + k^2 [\ell_{\text{ex}}^2 - \mathcal{B}(k)]\right)} \right]. \quad (14)$$

Equation (14) has a similar structure to the SW dispersion shown in Eqs. (34) and (35) of Ref. [45], inasmuch as the same approach was realized (small wave-vector limit). Nonetheless, such a reported SW dispersion is not strictly analytical since it requires the numerical integration of terms associated with the dipolar energy and, hence, the direct dependence with the NT geometry is lost. In the current case, the SW dispersion is fully analytical, and the role of the geometrical parameters is clearly identified. Thus, the SW dispersion shown in Eq. (14) is the first analytical expression reported so far when the dipolar interaction is taken into account. Such an equation allows us to obtain very simple expressions for (i) the frequency shift of two counterpropagating waves, (ii) the critical field that destabilizes the vortex state, and (iii) the ferromagnetic resonance frequency [$f(k=0)$]. These three concepts will be discussed in the next section.

III. RESULTS AND DISCUSSION

In the following discussion, permalloy (Py: Ni₈₀Fe₂₀) material is used for the calculations. Namely, the saturation magnetization is $M_s = 796$ kA/m, while the exchange constant is $A_{\text{ex}} = 13$ pJ/m. Also, the gyromagnetic ratio is $\gamma = 175.929$ GHz/T. A negative uniaxial anisotropy constant $K_u = -50$ kJ/m³ is used to stabilize the vortex ground state of the system [46], in the absence of an external circular field H_0 . Nonetheless, such easy-plane anisotropy or the applied circular field could be unnecessary if the tube length is finite with radii falling into the vortex state region [9]. Regarding the application of the DMM for thick nanotubes, the NT system is divided into N cylindrical layers where the thickness of each shell is $\zeta = 1$ nm. As a starting point, the approaches mentioned in Secs. II A, II B, II C, and II D are discussed for the cases $l = 0$, $a = 20$ nm, $d = 10$ nm, and $N = 10$. The numerical integration (case described in Sec. II A) along the azimuthal angle φ' and the radial coordinate ρ and ρ' [see Eq. (10)] allow us to calculate the spin-wave dispersion for thin NTs, which is presented in Fig. 2 (open circles). This result matches perfectly with the SW dispersion reported in Ref. [46], because the thickness is still small and the same parameters have been used. On the other side, the dashed black line in Fig. 2 describes the ultrathin approach described in Sec. II B, where even when the trend is very similar to the numerically calculated case (open circles), one can observe that the SW dispersion deviates for large positive wave vectors. Of course, such a deviation is expected since the product kd is large enough to fail the ultrathin approach.

Now, the ultrathin approach plus the dynamic matrix method summarized in Sec. II C is discussed. In this case, by using coupled cylindrical layers of thickness $\zeta = 1$ nm, the numerically calculated SW dispersion (open circles) is recovered, which is represented by the solid blue line depicted in Fig. 2. Note that the concordance between both methods

(numerical integration and ultrathin + DMM) confirms the validity of the combined use of the dynamic matrix method and the ultrathin approach, where the integrations along the NT thicknesses are avoided. Of course, the most crucial advantage of the ultrathin limit plus DMM is that it allows us to predict the magnonic spectra of thicker nanotubes (for small and large k) with high accuracy by taking into reasonable account the nonlocal nature of the demagnetizing fields. Finally, the approach shown in Sec. II D is also compared with the previous cases. In Fig. 2, the solid red line depicts the small- k limit case [Eq. (14)], where a good agreement is observed in the range $|k| < 10$ rad/ μm , that is, for $|k|d < 0.1$. Therefore, explicit expressions for the frequency shift Δf_{an} can be derived at the small wave vector limit, which will be analyzed in the following discussion.

In what follows, the ultrathin approach plus DMM are used to analyze the spin waves. The SW dispersion evaluated at $a = 20$ nm is shown in Fig. 3(a), where the tube thickness d is varied from 10 up to 40 nm. Here, it is seen that the nonreciprocity increases as the thickness increases, and for $d = 30$ and 40 nm the first high-order mode associated with the radial standing SWs is observed (dashed lines) in the considered frequency scale. In Fig. 3(b), the frequency shift $\Delta f = f(+\mathbf{k}) - f(-\mathbf{k})$ is shown, where one can observe that it scales linearly for small wave vectors, and then as k increases, Δf behaves nonmonotonically (see the solid lines). Such behavior has also been observed in synthetic antiferromagnets [38], where precisely the source of the nonreciprocity

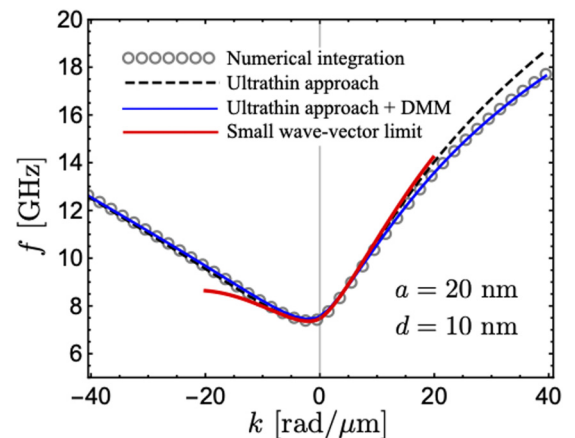


FIG. 2. Calculated spin-wave dispersion for a Permalloy nanotube with internal radius $a = 20$ nm and thickness $d = 10$ nm, showing the four theoretical approaches described in Sec. II. Open circles depict the spectra obtained through the numerical integration of Eq. (10), while the dotted line shows the ultrathin nanotube limit. The solid blue line illustrates the calculations based on the ultrathin NT limit and the dynamic matrix method (DMM). The solid red line shows the analytical dispersion obtained for the small wave-vector limit [see Eq. (14)].

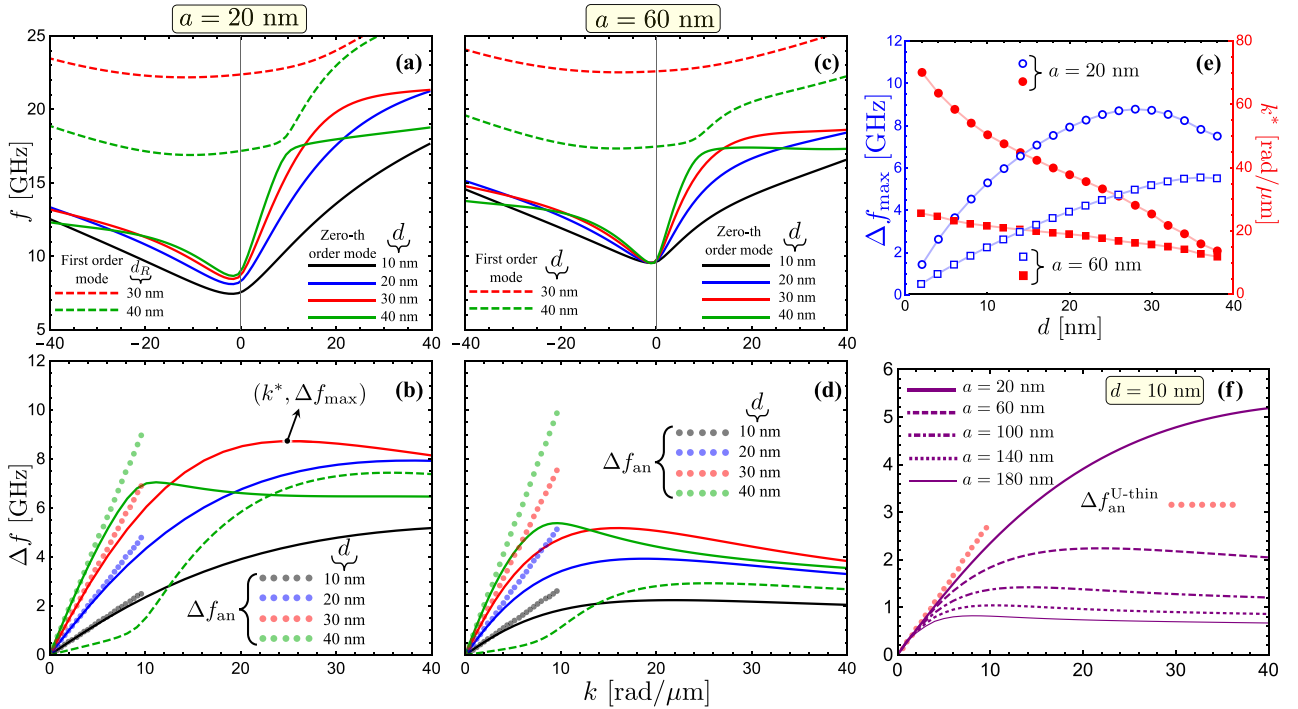


FIG. 3. Spin-wave dispersion and frequency shift for nanotubes with inner radius $a = 20$ nm [(a) and (b)] and $a = 60$ nm [(c) and (d)]. In both cases, the thickness d is varied from 10 up to 40 nm. In (b) and (d), the circles denote the analytical frequency shift Δf_{an} [see Eq. (15)]. Panel (e) shows the behavior of Δf_{max} (open symbols) and k^* (filled symbols) as a function of the NT thickness for $a = 20$ nm (circles) and $a = 60$ nm (squares), and (f) depicts the frequency shift Δf_{an} and $\Delta f_{\text{an}}^{\text{U-thin}}$ as a function of the wave vector for $d = 10$ nm and different a .

is the dipolar interaction. On the other side, the frequency shift in the small- k limit can be directly derived from Eq. (14), namely

$$\Delta f_{\text{an}} \approx \frac{\gamma \mu_0 M_s}{2\pi} kd \left[\frac{1}{2} + \frac{R+a}{4d} \ln \left(\frac{R}{a} \right) \right]. \quad (15)$$

In such a linear approximation of the frequency shift, the slope depends on both the thickness and the curvature. Circular dots in Fig. 3(b) show the behavior of Δf_{an} , where the easy-to-handle expression shown in Eq. (15) matches perfectly with the numerical calculations at small k , even for significant NT thicknesses. Therefore, although the linear approximation for Δf_{an} has been derived for thin NTs (assuming uniform radial magnetization profile), expression (15) is not restricted to thin curved structures. In the case $a = 60$ nm, the modes behave similarly to the previous case ($a = 20$ nm). Nevertheless, at $a = 60$ nm the low-frequency modes have almost the same frequency at zero wave vector [see Fig. 3(c)], which can be easily explained by using $f_{\text{an}}(k=0)$ in Eq. (14), i.e.,

$$f_{\text{an}}(0) = \frac{\gamma \mu_0}{2\pi} \sqrt{(H_0 + M_s) \left(H_0 + \frac{2|K_u|}{\mu_0 M_s} - \frac{\ell_{\text{ex}}^2 M_s}{aR} \right)}. \quad (16)$$

Note that the only term that depends on the radii is $-\ell_{\text{ex}}^2 M_s / (aR)$, thus as a (or $R > a$) increases, such a term becomes negligible and, hence, the $k = 0$ modes are excited at the same frequency. For instance, for $a = 20$ nm and $d = 40$ nm, the factor $\ell_{\text{ex}}^2 / (aR) \approx 0.04$, while for $a = 60$ nm and $d = 40$ nm, $\ell_{\text{ex}}^2 / (aR) \approx 0.01$. In other words, when the internal and external radii (a and R , respectively) are comparable with the

exchange length ℓ_{ex} , the SW modes, evaluated at zero wave vector, are strongly influenced by the NT geometry. Nevertheless, if $a \gg \ell_{\text{ex}}$ (or $R \gg \ell_{\text{ex}}$), the ferromagnetic resonance (FMR) modes are not influenced by the curvature anymore. It is worth noting that the FMR frequency shown in Eq. (16) allows us to obtain the critical field at which the vortex ground state becomes unstable. This field can be derived from the condition $f_{\text{an}}(k) = 0$ since, in such a case, the vortex state is no longer stable. For the magnetic nanotube, indeed, the minimum in frequency occurs at $k = 0$ (not shown), and then it is easy to see that the critical circular field is

$$H_c = \frac{\ell_{\text{ex}}^2}{aR} M_s - \frac{2|K_u|}{\mu_0 M_s}. \quad (17)$$

If the anisotropy is zero, the minimum field required to stabilize the vortex state is $\mu_0 H_c \approx 54$ mT, considering $a = 20$ nm and $R = 30$ nm. This result is consistent with the one reported in Ref. [82]. In the current system, the external field has been assumed zero; therefore, the critical condition to stabilize the vortex state requires that $|K_u| > A_{\text{ex}} / (aR)$.

On the other side, in Fig. 3(d), one can see that the maximum value of the frequency shift decreases as the inner radius a increases to 60 nm, which is in concordance with previously reported results [45]. The maximum of the frequency shift Δf_{max} and its respective wave vector k^* [illustrated in Fig. 3(b)] are presented in Fig. 3(e). One can observe that as the thickness of the NT increases, Δf_{max} (see the open circles and squares) behaves nonmonotonically, while the wave vector k^* (see the filled circles and squares) decreases. The nonmonotonicity of the frequency shift is explained due to

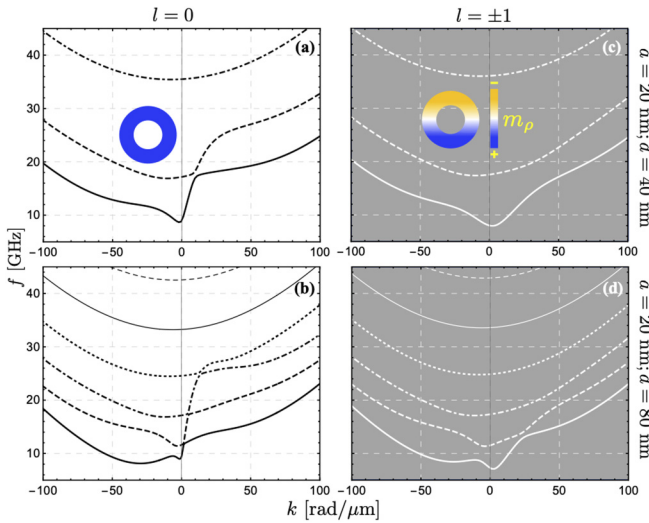


FIG. 4. Spin-wave dispersion for $l = 0$ [(a) and (b)] and $l = \pm 1$ [(c) and (d)] is calculated for an internal radius $a = 20$ nm and zero bias field. In the cases (a) and (c) the tube thickness is $d = 40$ nm, while in (b) and (d) $d = 80$ nm. The zero-, first-, second-, third-, fourth-, and fifth-order modes are shown through the solid, dashed, dot-dashed, dotted, thin, and thin-dashed lines, respectively. The insets in (a) and (c) denote the zero and first azimuthal order modes, respectively.

the coupling between the zeroth- and first-order modes. For large thicknesses, the high-order modes are excited at lower frequencies and, hence, once the fundamental and first-order modes hybridize, the nonreciprocal properties of the fundamental (zeroth-order) mode are depleted (see the discussion of Fig. 4). One interesting issue is that, at small wave vectors, Δf_{an} behaves in a similar way in the cases $a = 20$ and 60 nm [see the circular dots in Figs. 3(b) and 3(d)]. To explain the previous behavior, the analytical expression for Δf_{an} is further analyzed. In the case of an ultrathin NT, Δf_{an} can be expanded around $R = a$. Thus, it can be shown that

$$\Delta f_{\text{an}}^{\text{U-thin}} = \frac{\gamma \mu_0 M_s}{2\pi} kd. \quad (18)$$

Here, it is observed that the primary dependence of the frequency shift is associated with the NT thickness. Then, as the thickness increases, it can be demonstrated that a slight deviation around $\Delta f_{\text{an}}^{\text{U-thin}}$ occurs. Thereby, dipolar nonreciprocity at small wave vectors mainly depends on the NT thickness d . This explains the similar behavior of Δf_{an} in Figs. 3(b) and 3(d), because in both figures, the thicknesses are the same.

To complement the previous discussion, the behavior of Δf and $\Delta f_{\text{an}}^{\text{U-thin}}$ is analyzed for different internal radius a . Figure 3(f) depicts the calculated frequency shift (lines) and the linear approximation $\Delta f_{\text{an}}^{\text{U-thin}}$ (circles). Here, it is observed that the linear approximation given in Eq. (18) matches very well at small wave vectors. Of course, the analytical expression Δf_{an} in Eq. (15) is even better, inasmuch as it contains additional contributions associated with the curvature. Nevertheless, as mentioned before, both expressions Δf_{an} and $\Delta f_{\text{an}}^{\text{U-thin}}$ are similar since the main dependence comes from the NT thickness. Indeed, by defining the usual radii ratio as $\beta = a/R$, one can write $\Delta f_{\text{an}} = \eta(\beta)\Delta f_{\text{an}}^{\text{U-thin}}$, where

$\eta(\beta) = 1/2 + \frac{1+\beta}{4(1-\beta)} \ln(1/\beta)$. Such a function approaches 1 when $\beta \approx 1$, and it increases from it if β decreases beyond 0.5. As the internal radius increases, one can observe that the wave-vector range where the linear approximation $\Delta f_{\text{an}}^{\text{U-thin}}$ works is slightly reduced, which is not explicitly contained in Eq. (15). It is also observed that the curvature-induced frequency shift could be quite larger compared to the one measured in DM systems, around 1 or 2 GHz [55–58]. Returning to Eq. (18), one can note that the thickness dependence in $\Delta f_{\text{an}}^{\text{U-thin}}$ has the same characteristics as the one calculated for an antiferromagnetically coupled bilayer when the thicknesses of the ferromagnetic layers are ultrathin (see Eq. (7) in Ref. [38]). Hence, the asymmetric SW dispersion measured in ferromagnetic thin films coupled with heavy metals, where the Dzyaloshinskii-Moriya interaction is active, can be emulated for nanotubes in the regime of small wave vectors. Nevertheless, a crucial advantage of the spin waves in the tubular system is that the nonreciprocal properties are not restricted to thin structures. On the contrary, the SW asymmetry is enhanced as the thickness of the system increases. Moreover, due to the strongly asymmetric dipolar field of the curved magnetic system, there is no need for ultrathin FM films and heavy-metal layers to induce DM coupling, which undesirably increase magnetic damping and incorporate surface anisotropy. Instead, the chiral feature is provided by the classical dipole-dipole coupling.

Due to the geometrical characteristics of the NTs, azimuthal and radial standing spin waves can be excited. Azimuthal standing waves are associated with the confinement along the circumferential direction, which implicates the emergence of quantized modes that describe different azimuthal SW oscillations. The insets in Figs. 4(a) and 4(c) schematically show the states with $l = 0$ and ± 1 , respectively, where the normal magnetization component m_p is illustrated. It is worth mentioning that the excitation of modes with $l \neq 0$ depends on the external source. If a uniform excitation across the perimeter of the NT section is realized, waves with $l = 0$ will be driven, while a nonuniform spatial external excitation can stimulate standing modes with $l \neq 0$. On the other side, the radial standing waves are connected with the radial confinement of the system, and they are always present at high frequencies. A schematic representation of the zero and first azimuthal order mode is depicted in Figs. 4(a) and 4(c), respectively, for $a = 20$ nm and $d = 40$ nm. In Figs. 4(b) and 4(d) the thickness is increased to $d = 80$ nm, where it is evident that as the NT thickness increases, the radial standing modes are excited at lower frequencies, and hence these modes can hybridize with the low-frequency one. The main difference observed in the cases $l = 0$ and ± 1 is the behavior of the low-frequency mode, which is more asymmetric for the coherent azimuthal magnetization motion ($l = 0$) than the one calculated for $l = \pm 1$. Interestingly, Fig. 4 shows that in the range of frequency where the high-frequency modes do not interact with the fundamental one, the higher-order modes have a similar dispersion for both cases $l = 0$ and ± 1 , and even such higher-order radial standing waves exhibit a nonreciprocal SW dispersion.

To explain the dynamical behavior mentioned before, the exchange interaction is analyzed. From a qualitative point

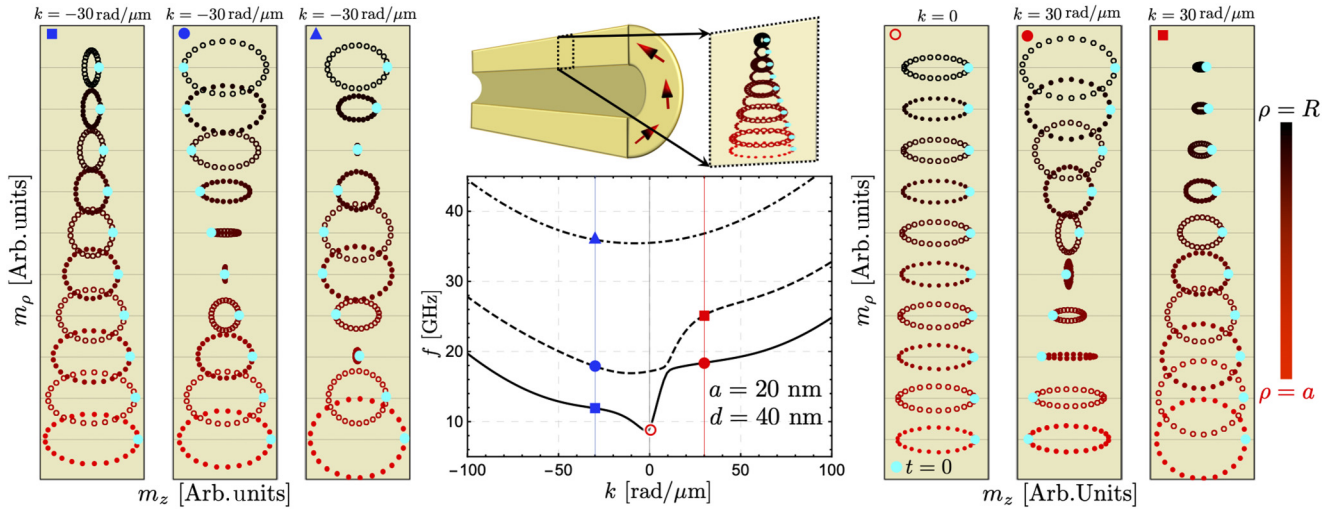


FIG. 5. Spin-wave profiles evaluated for the case $d = 40$ nm, $l = \pm 1$, and $a = 20$ nm. In the center of the figure, the SW dispersion is shown, where the (f, k) points (circles, squares, and triangles) indicate the states considered in the calculation of the SW spatial profiles. In the radial profiles, the red (black) color is associated with the nanotube's inner (outer) part. The cyan dots denote the $t = 0$ points, which allow us to observe the phase of the respective magnetization modes.

of view, as the thickness decreases, the dynamic magnetic moments have less space to describe their inhomogeneity, and hence large dynamical exchange energy is required to describe such a noncoherent magnetization motion, which implicates that the modes are excited at high frequencies. Nevertheless, as the thickness increases, the higher-order modes have more space to describe their motion, and therefore the frequency (or dynamical energy) is reduced. Thus, by comparing the azimuthal and radial modes of the nanotube system, the azimuthal oscillations have a more significant space to describe their spatial properties than the radial standing modes because the NT thickness is shorter than the NT perimeter. Thereby, in both cases $l = 0$ and ± 1 , the higher-order modes are dominated by the dynamical exchange energy correlated with the modulation of the dynamic magnetization along the thickness. Consequently, the frequencies of the higher-order modes evaluated at $l = 0$ and ± 1 are similar. Besides, one can note that the higher-order modes also have a nonreciprocal SW dispersion, but not as prominent as the Δf of the low-frequency mode, which is associated with the dynamic exchange interaction that dominates over the dynamic dipolar interaction.

In the following, the inhomogeneous radial characteristics of the magnetization dynamics are discussed. Figure 5 shows the magnetization profiles for the case $a = 20$ nm and $d = 40$ nm, and for different modes and wave vectors denoted by the symbols. At $k = 0$, the low-frequency mode describes an almost homogeneous profile along the NT thickness, and thereby the dynamic magnetization oscillates coherently with an approximately similar magnetization amplitude (see the open circle in Fig. 5). This quasihomogeneous profile of the modes evaluated at small wave vectors is expected since the dynamic dipole-dipole interaction between cylindrical layers is small at $k \rightarrow 0$, being zero at $k = 0$. Hence, the exchange interaction dominates and promotes a coherent oscillation with the same magnetization amplitude. Moreover, the homogeneous profile observed at $k = 0$ explains why the analytical

SW dispersion [see Eq. (14)] is also valid for thick nanotubes since, even when the analytical calculations are realized for thin NTs, the idea behind such a thin approach is the assumption that the amplitude of the dynamic magnetization is uniform along the thickness. On the other hand, as the wave vector increases, the classical dipole-dipole interaction becomes prominent, and the dynamic magnetization amplitude changes along the NT thickness. Basically, the dynamic magnetization compensates the dipolar field asymmetry by increasing its amplitude on one side of the nanotube. Thus, the outer ($\rho = R$) and inner ($\rho = a$) magnetic moments oscillate with different amplitudes, as shown in the magnetization profiles evaluated at $k = -30$ and 30 rad/ μm in Fig. 5 (see the blue and red squares). These results demonstrate that it is crucial to take into account the magnetization modulation along the thickness in the case of thick NTs, since if such a profile is not considered (homogeneous magnetization assumption), the frequency of the modes evaluated at $k \neq 0$ will be high because the spins are forced to oscillate with the same amplitude, which is not a state of the system. One can also note that the magnetization amplitude of the higher order modes is also modified along the thickness, which is seen in Fig. 5 for the cases $k = \pm 30$ rad/ μm (see the red and blue circles). Nevertheless, in general, it is observed that the higher-order modes have an almost reciprocal spin-wave dispersion, which is associated with the dynamic exchange interaction that dominates over the dynamic dipolar interaction, and also with the fact that the higher-order modes are more symmetric under inversion as compared with the modes localized at the inner or the outer cylindrical surfaces. The third mode (triangle) evaluated at $k = -30$ rad/ μm shows two nodes that are more asymmetric in amplitude with respect to the modes with one node. A similar behavior is given for the third mode evaluated at $k = +30$ rad/ μm (not shown).

It is worth mentioning that the radial modes in the tubular geometry share similarities with the perpendicular standing spin-wave modes in flat homogeneous films [88], or

the quantized SW modes in confined magnets [89], where the different modes are symmetrically quantized over the thickness at zero in-plane wave vector. For nonzero wave vectors, the modes are no longer symmetrically quantized, because they exhibit nodal lines shifted from the center of the film [90]. Such an asymmetric distribution of magnonic modes also occurs in inhomogeneous magnetic systems, such as graded-magnetization films [43,91], where the saturation magnetization changes across the thickness, and it is demonstrated here for the curvilinear geometry. The physical origin of the shifting of nodal lines is simply the inhomogeneity of the dipolar coupling in a confined magnetic nanostructure.

IV. CONCLUSIONS

The spin-wave spectra of a thick ferromagnetic nanotube in a vortex ground state have been theoretically addressed. It is found that the nonreciprocal features of the low-frequency in-phase modes are notoriously enhanced as the thickness of the nanotube increases, leading to a giant nonreciprocity, while the radial high-order modes still manifest a small nonreciprocal spin-wave dispersion. The profiles of the modes are analyzed and discussed, where it is evidenced that the

dipolar interaction induces inhomogeneous radial profiles at finite wave vectors. An analytical formula for the spin-wave dispersion at the small wave-vector limit is reported, which is nevertheless valid for thick nanotubes and allows us to derive simple expressions for (i) the critical field that destabilizes the vortex ground state, (ii) the ferromagnetic resonance, and (iii) the frequency shift of two counterpropagating spin waves. These simple analytical formulas are of the utmost importance for the scientific community concentrated on curvilinear magnonics since they describe the onset of the nonreciprocal effects induced by the classical dipole-dipole interaction, when the thickness of the nanotube increases beyond the 2D approach. The results are relevant for envisioning future applications associated with the asymmetric propagation of magnetic excitations in curvilinear nanostructures.

ACKNOWLEDGMENTS

The authors acknowledge financial support from Fondecyt, Grants No. 1210607 and No. 1201153, and Basal Program for Centers of Excellence, Grant No. AFB180001 CEDENNA, CONICYT. P.A.-S. acknowledges the support of CONICYT 22201272, and PIIC No. 043/2020.

-
- [1] R. Hertel, *J. Magn. Magn. Mater.* **249**, 251 (2002).
- [2] P. Landeros, S. Allende, J. Escrig, E. Salcedo, D. Altbir, and E. E. Vogel, *Appl. Phys. Lett.* **90**, 102501 (2007).
- [3] P. Landeros and A. S. Núñez, *J. Appl. Phys.* **108**, 033917 (2010).
- [4] M. Yan, C. Andreas, A. Kákay, F. García-Sánchez, and R. Hertel, *Appl. Phys. Lett.* **100**, 252401 (2012).
- [5] J. Otálora, J. López-López, P. Landeros, P. Vargas, and A. Núñez, *J. Magn. Magn. Mater.* **341**, 86 (2013).
- [6] D. D. Sheka, O. V. Pylypovskyi, P. Landeros, Y. Gaididei, A. Kákay, and D. Makarov, *Commun. Phys.* **3**, 128 (2020).
- [7] D. Makarov, O. M. Volkov, A. Kákay, O. V. Pylypovskyi, B. Budinská, and O. V. Dobrovolskiy, *Adv. Mater.* **34**, 2101758 (2021).
- [8] D. D. Sheka, *Appl. Phys. Lett.* **118**, 230502 (2021).
- [9] P. Landeros, O. J. Suarez, A. Cuchillo, and P. Vargas, *Phys. Rev. B* **79**, 024404 (2009).
- [10] A. Buchter, J. Nagel, D. Ruffer, F. Xue, D. P. Weber, O. F. Kieler, T. Weimann, J. Kohlmann, A. B. Zorin, E. Russo-Averchi, R. Huber, P. Berberich, A. Fontcuberta i Morral, M. Kemmler, R. Kleiner, D. Koelle, D. Grundler, and M. Poggio, *Phys. Rev. Lett.* **111**, 067202 (2013).
- [11] A. Buchter, R. Wölbing, M. Wyss, O. F. Kieler, T. Weimann, J. Kohlmann, A. B. Zorin, D. Ruffer, F. Matteini, G. Tütüncüoğlu, F. Heimbach, A. Kleibert, A. Fontcuberta i Morral, D. Grundler, R. Kleiner, D. Koelle, and M. Poggio, *Phys. Rev. B* **92**, 214432 (2015).
- [12] K. Baumgaertl, F. Heimbach, S. Maendl, D. Rueffer, A. Fontcuberta i Morral, and D. Grundler, *Appl. Phys. Lett.* **108**, 132408 (2016).
- [13] D. Vasyukov, L. Ceccarelli, M. Wyss, B. Gross, A. Schwarb, A. Mehlin, N. Rossi, G. Tütüncüoğlu, F. Heimbach, R. R. Zamani, A. Kovács, A. Fontcuberta i Morral, D. Grundler, and M. Poggio, *Nano Lett.* **18**, 964 (2018).
- [14] R. Streubel, P. Fischer, F. Kronast, V. P. Kravchuk, D. D. Sheka, Y. Gaididei, O. G. Schmidt, and D. Makarov, *J. Phys. D* **49**, 363001 (2016).
- [15] R. Hertel, *J. Phys.: Condens. Matter* **28**, 483002 (2016).
- [16] A. Fernández-Pacheco, R. Streubel, O. Fruchart, R. Hertel, P. Fischer, and R. P. Cowburn, *Nat. Commun.* **8**, 15756 (2017).
- [17] M. Staño and O. Fruchart, *Handbook Magn. Mater.* **27**, 155 (2018).
- [18] M. P. Proenca, C. T. Sousa, J. Ventura, and J. P. Araujo, in *Magnetic Nano- and Microwires*, 2nd ed., Woodhead Publishing Series in Electronic and Optical Materials, edited by M. Vázquez (Woodhead, Sawston, 2020), pp. 135–184.
- [19] M. Poggio, in *Magnetic Nano- and Microwires*, 2nd ed., Woodhead Publishing Series in Electronic and Optical Materials, edited by M. Vázquez (Woodhead, Sawston, 2020), pp. 491–517.
- [20] Z. K. Wang, H. S. Lim, H. Y. Liu, S. C. Ng, M. H. Kuok, L. L. Tay, D. J. Lockwood, M. G. Cottam, K. L. Hobbs, P. R. Larson, J. C. Keay, G. D. Lian, and M. B. Johnson, *Phys. Rev. Lett.* **94**, 137208 (2005).
- [21] A. Mehlin, B. Gross, M. Wyss, T. Schefer, G. Tütüncüoğlu, F. Heimbach, A. Fontcuberta i Morral, D. Grundler, and M. Poggio, *Phys. Rev. B* **97**, 134422 (2018).
- [22] M. Zimmermann, T. N. G. Meier, F. Dirnberger, A. Kákay, M. Decker, S. Wintz, S. Finizio, E. Josten, J. Raabe, M. Kronseder, D. Bougeard, J. Lindner, and C. H. Back, *Nano Lett.* **18**, 2828 (2018).
- [23] R. Hertel and J. Kirschner, *J. Magn. Magn. Mater.* **278**, L291 (2004).
- [24] H.-G. Piao, J.-H. Shim, D. Djuhana, and D.-H. Kim, *Appl. Phys. Lett.* **102**, 112405 (2013).

- [25] S. Da Col, S. Jamet, N. Rougemaille, A. Locatelli, T. O. Montes, B. S. Burgos, R. Afid, M. Darques, L. Cagnon, J. C. Toussaint, and O. Fruchart, *Phys. Rev. B* **89**, 180405(R) (2014).
- [26] M. Yan, C. Andreas, A. Kákay, F. García-Sánchez, and R. Hertel, *Appl. Phys. Lett.* **99**, 122505 (2011).
- [27] S. J. Son, X. Bai, and S. B. Lee, *Drug Discovery Today* **12**, 650 (2007).
- [28] V. K. Varadan, L. Chen, and J. Xie, Magnetic nanotubes and their biomedical applications, in *Nanomedicine* (Wiley, Chichester, 2008), pp. 273–327.
- [29] X. L. Liu, Y. Yang, C. T. Ng, L. Y. Zhao, Y. Zhang, B. H. Bay, H. M. Fan, and J. Ding, *Adv. Mater.* **27**, 1939 (2015).
- [30] D. F. Gutierrez-Guzman, L. I. Lizardi, J. A. Otalora, and P. Landeros, *Appl. Phys. Lett.* **110**, 133702 (2017).
- [31] A. Barman, G. Gubbiotti, S. Ladak, A. O. Adeyeye, M. Krawczyk, J. Gräfe, C. Adelmann, S. Cotofana, A. Naeemi, V. I. Vasyuchka, B. Hillebrands, S. A. Nikitov, H. Yu, D. Grundler, A. V. Sadovnikov, A. A. Grachev, S. E. Sheshukova, J.-Y. Duquesne, M. Marangolo, G. Csaba *et al.*, *J. Phys.: Condens. Matter* **33**, 413001 (2021).
- [32] V. V. Kruglyak, S. O. Demokritov, and D. Grundler, *J. Phys. D* **43**, 264001 (2010).
- [33] R. Camley, *Surf. Sci. Rep.* **7**, 103 (1987).
- [34] K. Mika and P. Grünberg, *Phys. Rev. B* **31**, 4465 (1985).
- [35] P. Grünberg, *J. Appl. Phys.* **57**, 3673 (1985).
- [36] P. Grünberg, R. Schreiber, Y. Pang, M. B. Brodsky, and H. Sowers, *Phys. Rev. Lett.* **57**, 2442 (1986).
- [37] V. Sluka, T. Schneider, R. A. Gallardo, A. Kákay, M. Weigand, T. Warnatz, R. Mattheis, A. Roldán-Molina, P. Landeros, V. Tiberkevich, A. Slavin, G. Schütz, A. Erbe, A. Deac, J. Lindner, J. Raabe, J. Fassbender, and S. Wintz, *Nat. Nanotechnol.* **14**, 328 (2019).
- [38] R. A. Gallardo, T. Schneider, A. K. Chaurasiya, A. Oelschlägel, S. S. P. K. Arekapudi, A. K. Roldán-Molina, R. Hübner, K. Lenz, A. Barman, J. Fassbender, J. Lindner, O. Hellwig, and P. Landeros, *Phys. Rev. Appl.* **12**, 034012 (2019).
- [39] M. Ishibashi, Y. Shiota, T. Li, S. Funada, T. Moriyama, and T. Ono, *Sci. Adv.* **6**, eaaz6931 (2020).
- [40] E. Albisetti, S. Tacchi, R. Silvani, G. Scaramuzzi, S. Finizio, S. Wintz, C. Rinaldi, M. Cantoni, J. Raabe, G. Carlotti, R. Bertacco, E. Riedo, and D. Petti, *Adv. Mater.* **32**, 1906439 (2020).
- [41] M. Grassi, M. Geilen, D. Louis, M. Mohseni, T. Brächer, M. Hehn, D. Stoeffler, M. Bailleul, P. Pirro, and Y. Henry, *Phys. Rev. Appl.* **14**, 024047 (2020).
- [42] R. A. Gallardo, P. Alvarado-Seguel, A. Kákay, J. Lindner, and P. Landeros, *Phys. Rev. B* **104**, 174417 (2021).
- [43] R. A. Gallardo, P. Alvarado-Seguel, T. Schneider, C. Gonzalez-Fuentes, A. Roldán-Molina, K. Lenz, J. Lindner, and P. Landeros, *New J. Phys.* **21**, 033026 (2019).
- [44] J. A. Otálora, M. Yan, H. Schultheiss, R. Hertel, and A. Kákay, *Phys. Rev. Lett.* **117**, 227203 (2016).
- [45] J. A. Otálora, M. Yan, H. Schultheiss, R. Hertel, and A. Kákay, *Phys. Rev. B* **95**, 184415 (2017).
- [46] L. Körber, G. Quasebarth, A. Otto, and A. Kákay, *AIP Adv.* **11**, 095006 (2021).
- [47] L. Körber, M. Zimmermann, S. Wintz, S. Finizio, M. Kronseder, D. Bougeard, F. Dirnberger, M. Weigand, J. Raabe, J. A. Otálora, H. Schultheiss, E. Josten, J. Lindner, I. Kézsmárki, C. H. Back, and A. Kákay, *Phys. Rev. B* **104**, 184429 (2021).
- [48] R. Verba, V. Tiberkevich, E. Bankowski, T. Meitzler, G. Melkov, and A. Slavin, *Appl. Phys. Lett.* **103**, 082407 (2013).
- [49] M. Kataoka, *J. Phys. Soc. Jpn.* **56**, 3635 (1987).
- [50] D. Cortés-Ortuño and P. Landeros, *J. Phys.: Condens. Matter* **25**, 156001 (2013).
- [51] J.-H. Moon, S.-M. Seo, K.-J. Lee, K.-W. Kim, J. Ryu, H.-W. Lee, R. D. McMichael, and M. D. Stiles, *Phys. Rev. B* **88**, 184404 (2013).
- [52] Y. Iguchi, S. Uemura, K. Ueno, and Y. Onose, *Phys. Rev. B* **92**, 184419 (2015).
- [53] L. Udvardi and L. Szunyogh, *Phys. Rev. Lett.* **102**, 207204 (2009).
- [54] K. Zakeri, Y. Zhang, J. Prokop, T.-H. Chuang, N. Sakr, W. X. Tang, and J. Kirschner, *Phys. Rev. Lett.* **104**, 137203 (2010).
- [55] K. Di, V. L. Zhang, H. S. Lim, S. C. Ng, M. H. Kuok, J. Yu, J. Yoon, X. Qiu, and H. Yang, *Phys. Rev. Lett.* **114**, 047201 (2015).
- [56] J. Cho, N.-H. Kim, S. Lee, J.-S. Kim, R. Lavrijsen, A. Solignac, Y. Yin, D.-S. Han, N. J. J. van Hoof, H. J. M. Swagten, B. Koopmans, and C.-Y. You, *Nat. Commun.* **6**, 7635 (2015).
- [57] S. Tacchi, R. E. Troncoso, M. Ahlberg, G. Gubbiotti, M. Madami, J. Åkerman, and P. Landeros, *Phys. Rev. Lett.* **118**, 147201 (2017).
- [58] R. A. Gallardo, D. Cortés-Ortuño, R. E. Troncoso, and P. Landeros, *Three-dimensional Magnonics* (Jenny Stanford, Berlin, 2019), pp. 121–160.
- [59] K. Di, S. X. Feng, S. N. Piramanayagam, V. L. Zhang, H. S. Lim, S. C. Ng, and M. H. Kuok, *Sci. Rep.* **5**, 10153 (2015).
- [60] P. Alvarado-Seguel and R. A. Gallardo, *Phys. Rev. B* **100**, 144415 (2019).
- [61] J. Lan, W. Yu, R. Wu, and J. Xiao, *Phys. Rev. X* **5**, 041049 (2015).
- [62] N. Reiskarimian and H. Krishnaswamy, *Nat. Commun.* **7**, 11217 (2016).
- [63] I. Dzyaloshinsky, *J. Phys. Chem. Solids* **4**, 241 (1958).
- [64] T. Moriya, *Phys. Rev. Lett.* **4**, 228 (1960).
- [65] A. Fert, in *Metallic Multilayers*, Mater. Sci. Forum Vol. 59 (Trans Tech, Bâch, 1991), pp. 439–480.
- [66] H. Leblond and V. Veerakumar, *Phys. Rev. B* **70**, 134413 (2004).
- [67] R. Arias and D. L. Mills, *Phys. Rev. B* **63**, 134439 (2001).
- [68] D. Mills, in *Band-Ferromagnetism* (Springer, Berlin, 2001), pp. 297–319.
- [69] T. Das and M. Cottam, *J. Magn. Magn. Mater.* **310**, 2183 (2007).
- [70] T. K. Das and M. G. Cottam, *Surf. Rev. Lett.* **14**, 471 (2007).
- [71] S. Mendach, J. Podbielski, J. Topp, W. Hansen, and D. Heitmann, *Appl. Phys. Lett.* **93**, 262501 (2008).
- [72] F. Balhorn, S. Mansfeld, A. Krohn, J. Topp, W. Hansen, D. Heitmann, and S. Mendach, *Phys. Rev. Lett.* **104**, 037205 (2010).
- [73] F. Balhorn, S. Jeni, W. Hansen, D. Heitmann, and S. Mendach, *Appl. Phys. Lett.* **100**, 222402 (2012).
- [74] A. L. González, P. Landeros, and A. S. Núñez, *J. Magn. Magn. Mater.* **322**, 530 (2010).
- [75] T. K. Das and M. G. Cottam, *J. Appl. Phys.* **109**, 07D323 (2011).

- [76] T. K. Das and M. G. Cottam, *IEEE Trans. Magn.* **46**, 1544 (2010).
- [77] A. Kozhanov, D. Ouellette, M. Rodwell, S. J. Allen, D. W. Lee, and S. X. Wang, *J. Appl. Phys.* **109**, 07D333 (2011).
- [78] T. Nguyen and M. Cottam, *Surf. Sci.* **600**, 4151 (2006).
- [79] M. C. Giordano, K. Baumgaertl, S. Escobar Steinvall, J. Gay, M. Vuichard, A. Fontcuberta i Morral, and D. Grundler, *ACS Appl. Mater. Interfaces* **12**, 40443 (2020).
- [80] J. Yang, J. Kim, B. Kim, Y.-J. Cho, J.-H. Lee, and S.-K. Kim, *Phys. Rev. B* **94**, 024425 (2016).
- [81] J. Yang, J. Kim, B. Kim, Y.-J. Cho, J.-H. Lee, and S.-K. Kim, *J. Appl. Phys.* **123**, 033901 (2018).
- [82] J. A. Otálora, D. Cortés-Ortuño, D. Görlitz, K. Nielsch, and P. Landeros, *J. Appl. Phys.* **117**, 173914 (2015).
- [83] M. Grimsditch, L. Giovannini, F. Montoncello, F. Nizzoli, G. K. Leaf, and H. G. Kaper, *Phys. Rev. B* **70**, 054409 (2004).
- [84] L. Giovannini, F. Montoncello, F. Nizzoli, G. Gubbiotti, G. Carlotti, T. Okuno, T. Shinjo, and M. Grimsditch, *Phys. Rev. B* **70**, 172404 (2004).
- [85] Y. Henry, O. Gladii, and M. Bailleul, [arXiv:1611.06153](https://arxiv.org/abs/1611.06153).
- [86] The relation between J_{ex}^{np} and A_{ex} is obtained by realizing the continuous approach of the discrete interaction $\epsilon_{\text{ex}}^{np}$.
- [87] P. Landeros, J. Escrig, D. Altbir, M. Bahiana, and J. d'Albuquerque e Castro, *J. Appl. Phys.* **100**, 044311 (2006).
- [88] S. Demokritov, B. Hillebrands, and A. Slavin, *Phys. Rep.* **348**, 441 (2001).
- [89] J. Jorzick, S. O. Demokritov, C. Mathieu, B. Hillebrands, B. Bartenlian, C. Chappert, F. Rousseaux, and A. N. Slavin, *Phys. Rev. B* **60**, 15194 (1999).
- [90] G. Dieterle, J. Förster, H. Stoll, A. S. Semisalova, S. Finizio, A. Gangwar, M. Weigand, M. Noske, M. Fähnle, I. Bykova, J. Gräfe, D. A. Bozhko, H. Y. Musienko-Shmarova, V. Tiberkevich, A. N. Slavin, C. H. Back, J. Raabe, G. Schütz, and S. Wintz, *Phys. Rev. Lett.* **122**, 117202 (2019).
- [91] L. Fallarino, B. J. Kirby, and E. E. Fullerton, *J. Phys. D* **54**, 303002 (2021).